Taylor & Francis
Taylor & Francis Group

Cross-equatorial flow of grounded abyssal ocean currents

ALEXANDER KIM†, GORDON E. SWATERS*‡ and BRUCE R. SUTHERLAND†§

†Department of Physics, University of Alberta, Edmonton T6G 2G1, Canada
‡Department of Mathematical and Statistical Sciences, University of Alberta,
Edmonton T6G 2G1, Canada
§Department of Earth and Atmospheric Sciences, and Institute for Geophysical Research,
University of Alberta, Edmonton T6G 2G1, Canada

The cross-equatorial flow of grounded abyssal ocean currents in a differentially rotating meridional channel with parabolic bottom topography is examined. In particular, the dependence is determined of the cross-equatorial volume flux on the underlying flow parameters including the slope of the channel's walls s, the half-width of the channel l, the half-width and height of the abyssal current a and H, respectively, the magnitude of the rotation vector Ω, the Earth's radius R, and the reduced gravity g'. In addition, it is shown that the ratio between the width of the channel and the zonal wavelength of a narrow wave structure that is formed by the current in the equatorial region plays a crucial role in determining into which hemisphere the current flows after its interaction with the equator. It is found that some parameters (e.g. a and H) do not have any significant effect on the zonal wavelength, while variations in other parameters (e.g. l, s, Ω, R and g') change the zonal wavelength and, consequently, can dramatically alter the qualitative trans-equatorial behavior of the abyssal current. After examining an auxiliary model of a particle in a rotating equatorial channel, it is shown that the zonal wavelength of the equatorial wave is linearly proportional to the equatorial length scale defined as $L_{\mathrm{eq}} = \sqrt{g's/l}/\beta$, where $\beta = 2\Omega/R$ is the equatorial value of the beta-parameter.

Keywords: Cross-equatorial flows; Grounded abyssal ocean currents; Deep western boundary currents

1. Introduction

Thorough knowledge of ocean circulation is a key component in understanding global climate. One of the most important phenomena that take place in the world oceans are large-scale ocean currents, which are generated by many different processes such as, for example, wind, buoyancy, and Coriolis forces.

At high latitudes in the northern hemisphere cooled salty water sinks to the deep ocean forming the North Atlantic Deep Water (NADW). The Labrador and Norwegian/Greenland seas are the main source regions that supply the NADW. From here it flows southward, initially as a consequence of the Sverdrup vorticity balance, then in the form of the geostrophically balanced Deep Western Boundary Current (DWBC) (Cunningham *et al.* 2007, McCarthy *et al.* 2012).

In the North Atlantic, away from the source regions, the DWBC takes the form of a grounded abyssal current that flows towards the equator on the continental slope along the east coast

---

*Corresponding author. Email: gswaters@ualberta.ca

of North America. During their equatorward propagation some water in the abyssal current gradually increases in temperature, mixes with the overlying fluid and rises to the surface supplying the flows that carry it back to subpolar regions. This process helps to compensate for the excessive amount of heat acquired by the surface waters at low latitudes (Siedler *et al.* 2001, Samelson 2011).

Due to the constraints associated with the conservation of potential vorticity (PV), idealized inviscid models are not able to fully describe abyssal currents that cross the equator and propagate long distances away from it. Killworth (1991) has shown that inviscid cross-equatorial geostrophic adjustment allows the fluid to penetrate into the opposite hemisphere, but the penetration distance is limited to a few deformation radii from the equator. This raises the interesting theoretical question concerning ascertaining the dynamical processes that are responsible for the cross-equatorial motion of grounded abyssal currents.

Edwards and Pedlosky (1998) studied potential vorticity modification in the framework of nonlinear DWBCs. They pointed out that the relative vorticity in the abyssal currents is negligible and, since the Coriolis parameter changes sign at the equator, penetration into the opposite hemisphere by the abyssal currents can only occur if the PV is modified by dissipative or nonconservative processes.

Kawase *et al.* (1992) numerically integrated the three-dimensional equations of motion under the Boussinesq approximation assuming flat bottom topography. During the initial stages of its motion, the simulated current was observed to flow in the equatorward direction. According to this study, when the current enters the equatorial region it turns eastward and oscillates perpendicular to the equator. However, in the steady-state limit the oscillations disappear and the crossing of the equator is observed along the western boundary.

Another aspect, which we do not consider here, which may be important in the cross-equatorial dynamics of abyssal ocean currents is vertical structure. This has been examined by Nof and Olson (1993) and Choboter and Swaters (2003).

Borisov and Nof (1998) compared a relatively simple model of the inertial motion of particles to numerical simulations of eddies propagating in a parabolic meridional channel on an equatorial β-plane. Although models of particles and eddies have some important differences, Borisov and Nof (1998) found that the dependence of the cross-equatorial volume flux on the steepness of the channel walls was very similar in both models. They also concluded that the splitting of the eddies into northward and southward trajectories occurs because of the presence of the bathymetry and not due to the conservation of potential vorticity. The penetration into the opposite hemisphere was argued to be independent of the initial potential vorticity distribution. Thus, the modification of potential vorticity merely takes place to allow the current to follow paths prescribed to it by the shape of the bottom topography.

Nof and Borisov (1998) numerically simulated the cross-equatorial motion of a continuous double-front grounded current (flows with an upslope and downslope incropping or grounding in the height field) in a meridional channel with parabolic bottom topography on an equatorial β-plane. Their study showed that the percentage of volume flux that crossed the equator and ended up in the opposite hemisphere depends on the steepness of the bottom topography. In general, many similarities were found between the model of continuous currents and the models of eddies and particles studied by Borisov and Nof (1998). The particle simulations, however, occasionally exhibited chaotic behavior not observed in the cases of currents and eddies.

Choboter and Swaters (2000) examined both the frictional planetary-geostrophic and full shallow water equations in the context of abyssal cross-equatorial currents over idealized topography. The main disadvantage of their frictional planetary-geostrophic model lies in

neglecting the fluid inertia. However, after comparing this model to a more sophisticated shallow-water model they concluded that both models quantitatively agree in capturing certain important aspects of the motion such as along-shelf propagation, downhill acceleration and northward-southward splitting of the flow in the equatorial region.

Swaters (2013) derived a nonlinear planetary-geostrophic model for the hemispheric-scale flow of abyssal currents on a sloping bottom far from the equator on a rotating sphere and found an exact analytic solution. Further analysis of this solution revealed several interesting properties: the groundings of the current, i.e. the curves along which the current height intersects the bottom, were found to be set by the boundary conditions and do not change as the current propagates equatorward; the averaged height of the current showed a nearly linear decrease as the current approaches the equator, while the meridional volume transport was shown to be independent of latitude. The main disadvantage of the solution was its singularity at the equator. Hence, this model is incapable of describing the behavior of the abyssal current as it encounters the equator.

The principal goal of this paper is to model the equatorward propagation of a grounded abyssal current in a differentially rotating meridional channel with parabolic bottom topography that spans the equator. In this sense, we will resolve the singularity in the Swaters (2013) solution and provide a detailed description of the dependence of the cross-equatorial volume flux on all the flow parameters. It is observed that the initially equatorward flowing grounded abyssal current turns eastward and accelerates downslope when it enters the vicinity of the equator. After travelling in the eastward direction and oscillating perpendicular to the equator, the abyssal current rises on the opposite eastern side of the topography reaching its maximum run-up point and then ends up in the southern or northern hemisphere depending on the physical parameters.

While there are similarities between the study we present here and the modeling described in Nof and Borisov (1998), our work differs in at least three aspects. Nof and Borisov's (1998) theoretical modeling was based on assuming that the flow away from the equator possessed constant PV with an abyssal height field and geostrophically balanced meridional or along slope velocity that depended only parametrically on latitude, and with no compensating cross-slope velocity that is required to balance the latitudinal planetary vorticity gradient. All three of these conditions are relaxed here. The midlatitude flow is not assumed to possess constant potential vorticity everywhere, and the dependence of the flow in midlatitudes on the planetary vorticity gradient is dynamically determined and the abyssal current possesses a small but necessary cross-slope velocity in midlatitudes.

In particular it is shown that the position of the maximum run-up point relative to the crest and troughs of the zonal wave in the equatorial region is ultimately responsible for determining into which hemisphere the current will flow. It is also shown that a model of a particle in a rotating cross-equatorial channel is capable of explaining several important properties of the equatorial structure and cross-equatorial flow of grounded abyssal currents.

The plan of this paper is as follows. Section 2 presents the equations and boundary conditions that are used in the numerical simulations, as well as describing the geometry of the problem. Section 3 describes the results of the numerical simulations. Section 4 introduces a simplified model of a particle in an equatorial channel is that is very useful in understanding various aspects of the numerical simulations. Section 5 further discusses the results and makes qualitative estimates using oceanographically observed estimates for the order of magnitudes for the parameters of deep currents in the North Atlantic and makes some concluding remarks and suggestions for further research.
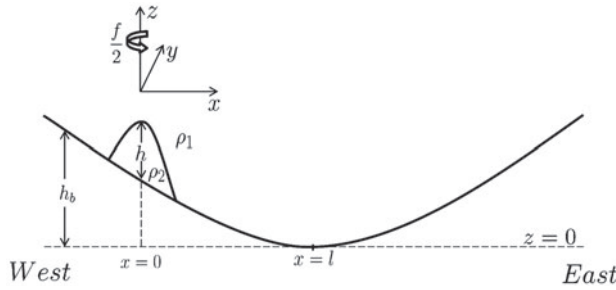
Figure 1.   Geometry of this model. The west-to-east cross-section along $y = y_0$. h_b is the bottom topography, h is the abyssal current thickness (lower layer), $\rho_{1,2}$ are the densities in the upper and lower layers, respectively. The center of the current is located at $x = 0$. The point of maximum depth is located at $x = l$.

2. Numerical model and geometry

We work with a two-layer reduced-gravity model that assumes that the density in the upper layer is equal to a constant ρ_1 and the density in the lower layer is given by a constant ρ_2 with stable stratification (i.e. $\rho_2 > \rho_1$). Furthermore, the upper layer is assumed to be infinitely deep and motionless. The geometry of the problem is shown in figure 1. It shows the west-to-east cross-section view at the initial location of the current located at $y = y_0$, where y increases in the northward direction and $y = 0$ corresponds to the equator. Although it is possible to work in spherical coordinates, for convenience, we work in Cartesian coordinates. The positive x and z directions point eastward and vertically upward, respectively. The positive y direction points northward.

The reduced-gravity shallow water equations, with horizontal friction, are given by

$$u_t + uu_x + vu_y - fv = -g'(h + h_b)_x + \text{Fric}_x, \tag{1a}$$

$$v_t + uv_x + vv_y + fu = -g'(h + h_b)_y + \text{Fric}_y, \tag{1b}$$

$$h_t + (hu)_x + (hv)_y = 0, \tag{1c}$$

$$p = \rho_2 g'(h + h_b), \tag{1d}$$

in which subscripts denote partial derivatives (unless otherwise denoted, e.g. the friction terms), $u(x, y, t)$ and $v(x, y, t)$ are the eastward and northward velocities, respectively, $p(x, y, t)$ is the dynamic pressure in the abyssal current, $g' \equiv (\rho_2 - \rho_1)g/\rho_2 > 0$ is the reduced gravity, $f = 2\Omega \sin(y/R)$ is the Coriolis parameter where $\Omega = 2\pi$ rads/day is Earth's angular frequency and R is the radius of the Earth, $h(x, y, t)$ is the height of the abyssal current above the zonally varying topography, which is given by $h_b(x)$. Rather than making the usual equatorial β-plane approximation in which $2\Omega \sin(y/R)$ is Taylor expanded as $2\Omega \sin(y/R) \approx 2\Omega y/R = \beta y$, we have chosen to retain the full trigonometric representation because our domain extends into midlatitudes and we wanted a uniformly valid and bounded representation for the Coriolis parameter (see also Choboter and Swaters 2004, Swaters submitted for publication).

We assume the viscosity terms to be given by

$$\left(\text{Fric}_x, \text{Fric}_y\right) = \nu \nabla \cdot \left[h \nabla (u, v)\right]/h, \tag{2}$$

as described by Gustafsson and Sundstrom (1978) where ν is a "viscosity" coefficient. According to Gent (1993), this form of the viscosity term is energetically consistent unlike the

other commonly used form $\nu\nabla^2\boldsymbol{u}$ (e.g. Lorenz 1980, Gent and McWilliams 1982, Curry and Winsand 1986).

It is important to point out that we have not included either a bottom friction term or a diapycnal mixing term in (1a,b) or (1c). It is not unreasonable to assume that bottom friction or vertical mixing might be physically important in the dynamics of grounded abyssal flows near the equator. It is noted that Gent (1993) has provided an energetically consistent formulation of diapycnal mixing in the single-layer shallow water equations. It is further noted that the form of the friction terms assumed in (2) is, however, sufficient to ensure the existence and smooth regularity of solutions to the initial value problem associated with (1a–c) (Gustafsson and Sundstrom 1978). Nof and Borisov (1998) did not include either of these effects in their numerical modeling. Since part of our analysis is focused on building on and comparing our results with those of Nof and Borisov (1998) we have chosen not to include these effects in our study as well. Nevertheless, the role of bottom friction and diapycnal mixing in the cross-equatorial dynamics of grounded abyssal currents certainly deserves further study and this is left for another contribution. For example, Swaters (submitted for publication) has shown how bottom friction can have an important role in determining the leading order structure of the height of equator-crossing grounded abyssal currents in the equatorial dissipation zones needed for the required PV adjustment.

The resulting system of equations can be written in the conservation form, given by

$$\boldsymbol{q}_t + \boldsymbol{F}_x + \boldsymbol{G}_y = \boldsymbol{S}^b + \boldsymbol{S}^c + \boldsymbol{S}^\nu, \tag{3}$$

where

$$\boldsymbol{q} = \begin{pmatrix} h \\ hu \\ hv \end{pmatrix}, \qquad \boldsymbol{F} = \boldsymbol{q}u = \begin{pmatrix} hu \\ hu^2 \\ huv \end{pmatrix}, \qquad \boldsymbol{G} = \boldsymbol{q}v = \begin{pmatrix} hv \\ huv \\ hv^2 \end{pmatrix}, \tag{4a–c}$$

$$\boldsymbol{S}^b = \begin{pmatrix} 0 \\ -g'h(h+h_b)_x \\ -g'h(h+h_b)_y \end{pmatrix}, \quad \boldsymbol{S}^c = \begin{pmatrix} 0 \\ 2\Omega\sin(y/R)\,hv \\ -2\Omega\sin(y/R)\,hu \end{pmatrix}, \quad \boldsymbol{S}^\nu = \begin{pmatrix} 0 \\ \nu\nabla\cdot(h\nabla u) \\ \nu\nabla\cdot(h\nabla v) \end{pmatrix}. \tag{4d–f}$$

We use a finite volume method to discretize the above equations in order to solve them numerically. This scheme was initially developed by McDonald (1971) and MacCormack and Paullay (1972) to solve the two-dimensional shallow water equations. We divide our domain into a number of nonoverlapping regions (finite volumes) in such a way that every nodal point is located inside a region. The differential equations are then integrated over each finite volume. Piecewise constant profiles are used to calculate integral quantities that describe the change of the dependent physical variable between the nodal points. Finally, we arrive at discrete analogs of our differential equations that contain values of the dependent variables at several nodal points (for details see Kim 2013).

A staggered Arakawa C-grid (Arakawa and Lamb 1977, Arakawa and Hsu 1990) is implemented in our model. This grid is frequently used in numerical simulations of fluid flow (e.g. Nof and Borisov 1998, Stephens and Marshall 2000, Choboter and Swaters 2004) and is a very suitable choice for our version of the shallow water equations.

We restrict attention to a parabolically shaped grounded abyssal current initially located on the western side of the topography and centered at $x = 0$ km and located on the northern
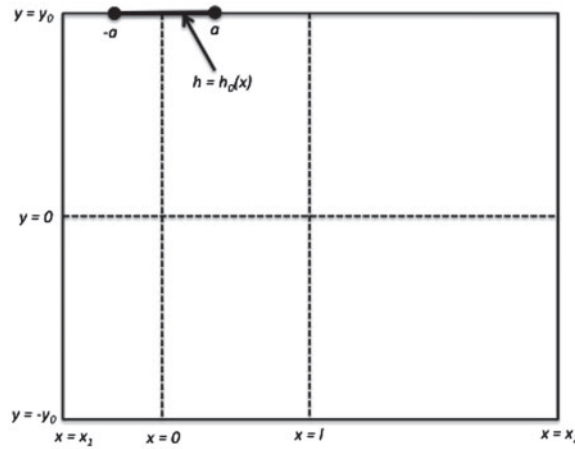
Figure 2.   Domain used in the numerical simulations. The boundaries of the domain are located along $y = \pm y_0$ and $x = x_{1,2}$ with $x_1 > x_2$, respectively. The initial current height $h_0(x)$ and northward velocity $v_0(x)$ are only nonzero along $y = y_0$ for $|x| < a$. Zero flux boundary conditions are assumed for u, v and h everywhere else on the boundaries in the numerical simulations. The center of the initial current is located at $x = 0$. The distance between the center of the initial current and the point of maximum depth is l.

boundary $y_0 = 3000$ km, which corresponds to approximately 27° N. The height of the inflow current is given by

$$h(x, y_0) = h_0(x) \equiv \begin{cases} H(1 - (x/a)^2) & \text{for } |x| \le a, \\ 0 & \text{for } |x| > a, \end{cases} \tag{5}$$

where H is the maximum height of the initial current in meters and a is its half-width in kilometers. The bottom topography is modeled as the parabola

$$h_b(x) = \frac{sx^2}{2l} - sx, \tag{6}$$

where

$$s = -\frac{1}{2a} \int_{-a}^{a} \partial_x h_b \, \mathrm{d}x > 0, \tag{7}$$

is the average slope (measured positively for decreasing topographic height) of the topography below the initial inflow current. Estimates for the value of s can be determined by observations (e.g. Sandoval and Weatherly 2001, Swaters 2006). The distance between the center of the current height $h_0(x)$, located at $x = 0$, and point of the maximum depth is given by l (see figure 1). The spatial domain used in our numerical simulations is depicted in figure 2.

Previous attempts to simulate cross-equatorial abyssal flows (e.g. Borisov and Nof 1998, Nof and Borisov 1998, Choboter and Swaters 2000, 2003) showed that after the current reaches the equator it moves eastward while oscillating meridionally until reaching the eastern side of the basin. The resulting outflow can move meridionally into either hemisphere. The location and structure of the outflow current is not known in advance, and therefore our boundary conditions should not have any effect on the motion inside of the domain. For these reasons, we used open boundary conditions (e.g. Stevens 1990, Kirkpatrick and Armfield 2009) for all four boundaries, which means that the normal component of the spatial gradient of the abyssal current height h and the velocities (u, v) are equal to zero on the boundaries located at
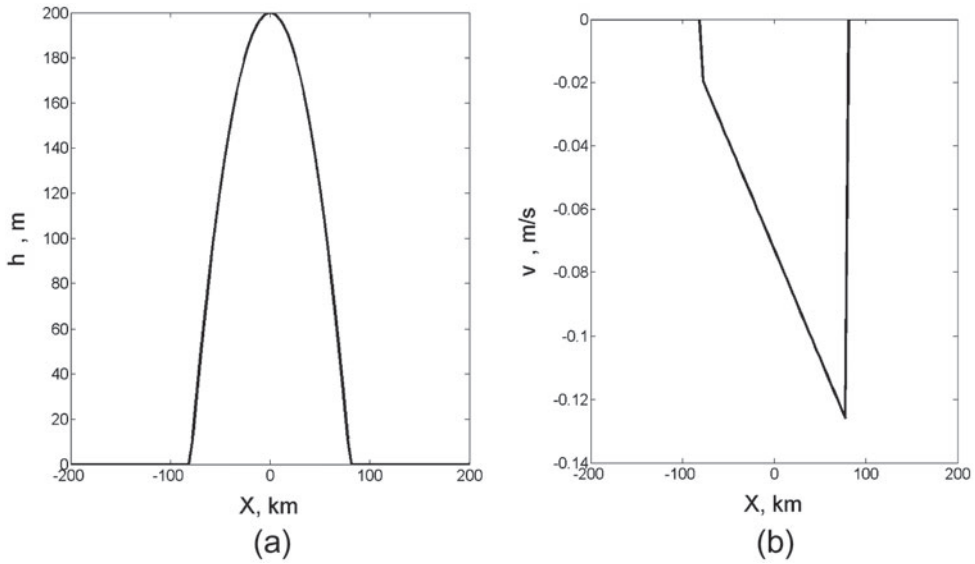
Figure 3. (a) Current height h_0 along $y = y_0$. (b) Northward velocity v_0 along $y = y_0$.

$y = \pm y_0$ and $x = x_1, x_2$, respectively. It is important to point out that along $y = y_0$ these zero normal flux conditions only apply for $|x| > a$ (i.e. outside the inflow boundary region). Along $y = y_0$ in the interval $|x| \le a$ (i.e. the inflow boundary region), Dirichlet boundary conditions for h and the velocities (u, v) (described below) are explicitly prescribed, which corresponds to the inflow abyssal current.

The shape of the current's height h along the inflow boundary is given by (5) as shown in figure 3(a). However, to initialize the numerical code we also need to know the inflow boundary conditions for the other two unknown variables u and v. In order to obtain them, we make use of the geostrophic balance approximation, which implies that in midlatitudes the main balance occurs between the slope-induced gravitational force and the Coriolis force.

The geostrophic balance equations at $y = y_0$ are obtained from our system of shallow water equations by neglecting the acceleration terms in the x- and y-momentum equations, i.e.

$$2\Omega \sin (y_0/R) (v, u) = g' (\partial_x, -\partial_y) (h_b + h). \tag{8}$$

Thus, the geostrophic equations allow us to complete our set of boundary conditions at $y = y_0$

$$h(x, y_0) = h_0(x), \tag{9a}$$

$$v(x, y_0) = v_0(x) \equiv \begin{cases} (v_{\text{nof}}/s) \, \partial_x(h_b + h_0) & \text{for } |x| \le a, \\ 0 & \text{for } |x| > a, \end{cases} \tag{9b}$$

$$u(x, y_0) = 0, \tag{9c}$$

in which we have defined

$$v_{\text{nof}} \equiv g's/f_0, \tag{10}$$

to be the *Nof speed* that is determined by a balance between the Coriolis and the gravitational forces over a topographic slope s for a grounded abyssal current (Nof 1983), where the Coriolis parameter $f_0 \equiv 2\Omega \sin(y_0/R)$. Even though we prescribe the cross-slope velocity u to be zero along the inflow boundary our numerical solution will clearly show that a small but nonzero

Table 1.   Default values of the physical parameters.

Variable	Description	Default value
H	Maximum current height	200 m
a	Current half-width	80 km
s	Average slope parameter below current	6×10^{-3}
l	Distance between current center and point of maximum depth	1000 km
g'	Reduced gravity	8×10^{-4} m/s^2
Ω	Angular frequency of Earth's rotation	7.29×10^{-5} rad/s
ν	Viscosity coefficient	100 m^2/s
R	Radius of Earth	6371 km
ϕ_0	Initial latitude	27° N
y_0	$y_0 = R\phi_0$	3000 km
x_1	Western boundary of domain	−500 km
x_2	Eastern boundary of domain	2500 km

cross-slope velocity is generated in midlatitudes (required to compensate for the variable Coriolis parameter).

In this paper, unless otherwise specified, we will use the control parameter values given in table 1. They are estimated from observations (e.g. De Madron and Weatherly 1994, Sandoval and Weatherly 2001, Swaters 2006). Assuming these values, it follows that $(h_b + h_0)_x < 0$ and it therefore follows that the initial meridional velocity $v_0(x)$ is strictly negative for $|x| \leq a$. As shown by Swaters (2013, submitted for publication), this condition ensures, in the inviscid steady-state nonlinear planetary geostrophic limit, that no shock forms in the solution prior to it encountering the equator. Figures 3(a) and (b) show the cross-section view of the current's height h_0 and its corresponding meridional velocity v_0 along the northern inflow boundary, respectively.

3. Description of the numerical simulations

During the initial stages of its motion the current is seen to propagate along the continental slope with almost no change in the location of its groundings at $x = \pm a$ (see figure 4(a)) consistent with the theoretical predictions of Swaters (2013, submitted for publication). Upon entering the equatorial region the fluid forms a narrow current where frictional effects play a nonnegligible role. (Swaters (submitted for publication) has recently completed a comprehensive theoretical asymptotic/boundary layer analysis for equator-crossing grounded abyssal currents and has shown that friction makes a leading order contribution to the dynamics in relatively meridionally narrow O (3 km) zonally elongated O (165 km) discrete bands located within an otherwise "inner" inertial equatorial boundary layer of meridional width O (220 km) centered on the equator.)

The current slightly overshoots the equator while it flows in the downslope direction, then it gradually returns back to the northern hemisphere as it passes the line of the maximum depth at $x = 1000$ km. Subsequently, the fluid rises up on the opposite side of the topography and begins to head southward as it reaches the point of a maximum run-up (eastern most point in the equatorial region) (see figure 4(b)). Thereafter, the current increases its height and width as it leaves the vicinity the equator. In this particular simulation, the entire current eventually ends up propagating southward on the eastward side of the topography in the southern hemisphere (see figure 4(c)).
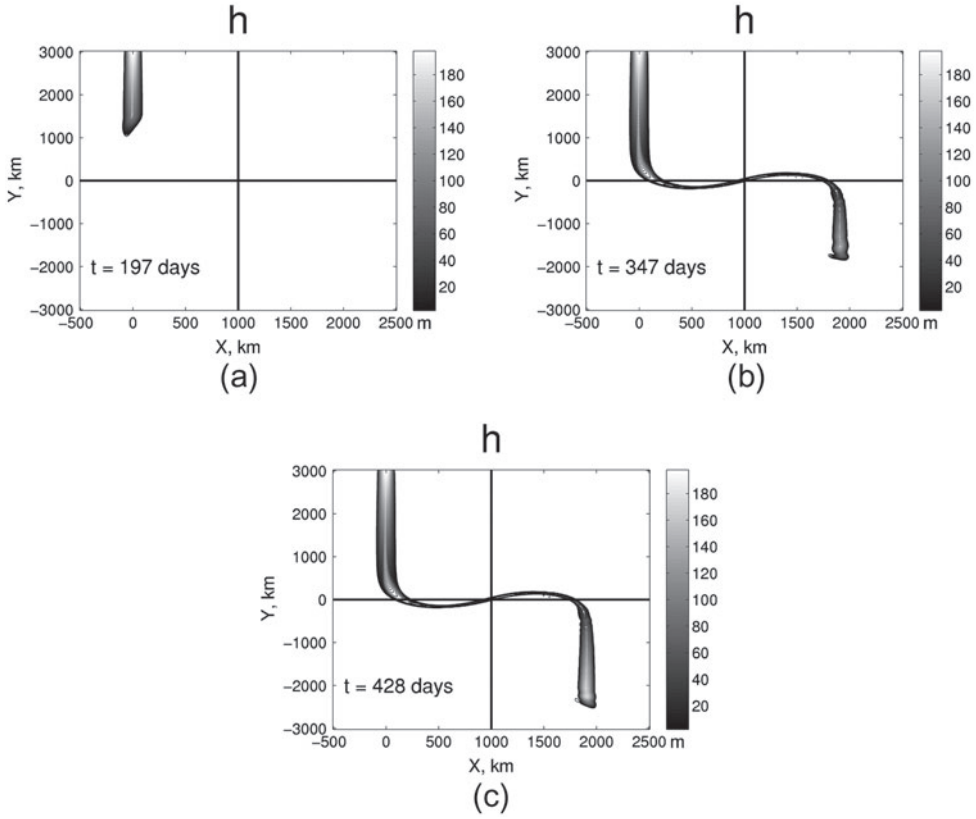
Figure 4. Instantaneous contour plots of *h* for the simulation assuming the default parameters values listed in table 1. The horizontal line marks the equator. The vertical line marks the location of the point of greatest ambient depth. The grayscale is proportional to the magnitude of *h* and illustrates the localized variation in the height as the current encounters the equator. Figures 4(a)–(c) show *h* at *t* = 197, 347 and 428 days, respectively.

The increase of the total energy, E, and mass, M, of the current with time within the computational domain is shown in figure 5, where

$$E \equiv \frac{1}{2} \iint \rho_2 \left[h \left(u^2 + v^2 \right) + g'(h + h_{\mathrm{b}})^2 - g'h_{\mathrm{b}}^2 \right] \, \mathrm{d}x \, \mathrm{d}y, \tag{11a}$$

$$M \equiv \iint \rho_2 h \, \mathrm{d}x \, \mathrm{d}y. \tag{11b}$$

Both graphs show almost linear growth until $t \approx 500$ days, when the flow reaches the southern boundary on the eastern side of the channel. After this moment we consider the current to be at a near steady state, which is characterized by the relatively constant values of mass and energy in the domain.

In order to provide an "averaged-over-time" description of the flow we averaged the solutions over the time period $T_1 \leq t \leq T_2$, where T_1 is the moment in time when both the total energy and mass initially reach their more-or-less constant level (see figure 5) and $T_2 > T_1$ is the final time of our simulations. The precise values of T_1 and T_2 used depended on the particular simulation.
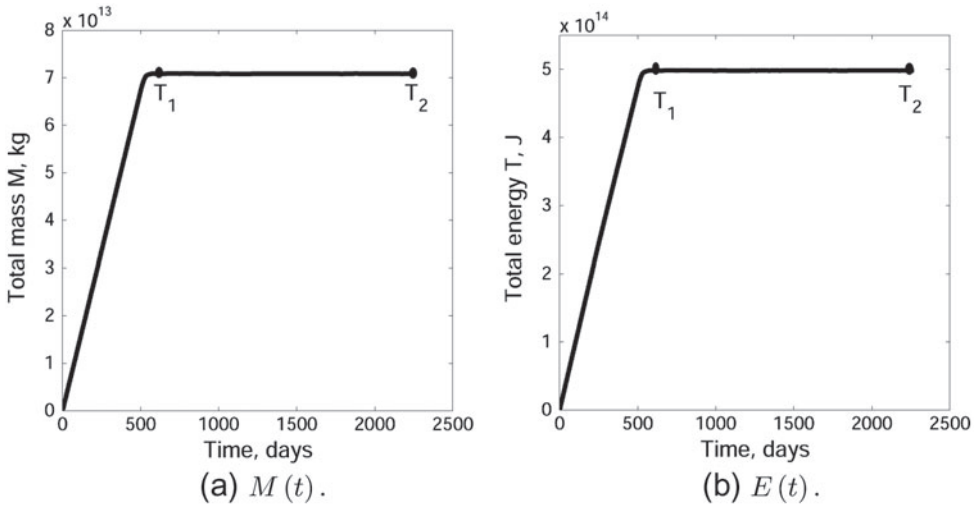
Figure 5. (a) Total mass M in kg and (b) total energy E in Joules for the simulation for the default parameter values in table 1.

Contour plots of the time averaged solutions h_{av}, u_{av} and v_{av} defined as

$$(h, u, v)_{av} \equiv \frac{1}{T_2 - T_1} \int_{T_1}^{T_2} (h, u, v) (x, y, t) \, dt, \tag{12}$$

are depicted in figures 6(a)–(c), respectively. Because the eastward speed, $|u_{av}|$, is significantly less in midlatitudes than in the equatorial region, its contours are not visible away from the equator (see figure 6(b)). Note that we consider the "noise" seen in u_{av} and v_{av} in the southern hemisphere in figures 6(b) and (c) to be numerical artifacts which arise on account of the fact that we tried to run the simulations with a low value of the viscosity.

It is observed that in the northern hemisphere the thickness of the abyssal current decreases with the latitude almost linearly, consistent with properties of the Swaters (2013, submitted for publication) solution to the associated planetary geostrophic model. In terms of the Cartesian coordinates used here, the Swaters (2013, submitted for publication) planetary geostrophic model can be written in the form

$$v = \frac{g'}{f(y)}(h + h_b)_x, \qquad u = -\frac{g'}{f(y)}h_y, \qquad (hu)_x + (hv)_y = 0. \tag{13a–c}$$

If the geostrophic relations (13a,b) are substituted into the mass conservation equation (13c), it follows that h satisfies the quasi-linear hyperbolic equation

$$\frac{f}{f_y}h_y - \frac{h}{\partial_x h_b}h_x = h, \tag{14}$$

which has the implicit solution $h = h_p(x, y)$ given by

$$h_p(x, y) = \frac{f}{f_0}h_0(\tau), \tag{15}$$

$$h_b(\tau) + (f_0 - f)\frac{h_0(\tau)}{f_0} = h_b(x). \tag{16}$$
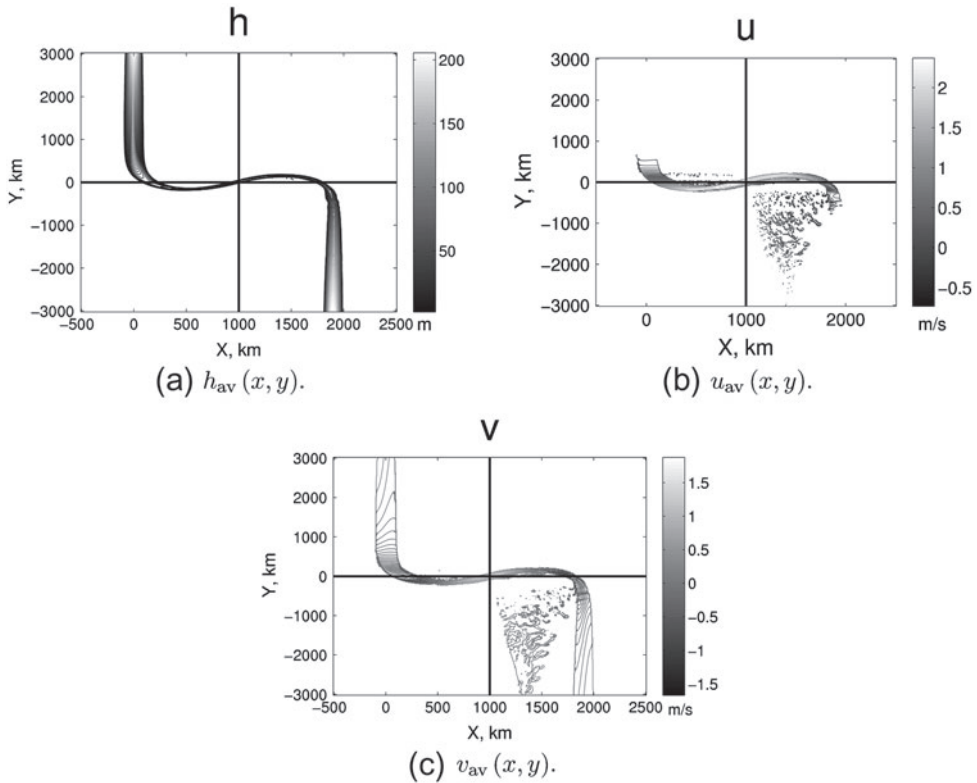
Figure 6. Contour plots of (a) $h_{av}(x, y)$, (b) $u_{av}(x, y)$, and (c) $v_{av}(x, y)$, respectively, for the simulation assuming the default parameters values listed in table 1. The grayscale is proportional to the amplitude of the individual field in each panel and illustrates the localized variability as the equator is encountered.

This solution satisfies $h_p(x, y_0) = h_0(x)$. In practice one obtains $h_p(x, y)$ as follows. Given the coordinates (x, y), $\tau(x, y)$ is obtained by solving for τ from (16) and then substituting into the right-hand side of (15) to determine $h_p(x, y)$. In general, solving for τ from (16) must be done numerically. However, for our particular choice of $h_0(x)$ and $h_b(x)$, given by (5) and (6), respectively, there exists an explicit analytical solution (see Swaters 2013, submitted for publication) for τ as a function of (x, y).

Figures 7(a) and (b) show the heights h_p and h_{av} obtained from the planetary geostrophic model approximation and the fully nonlinear numerical simulations, respectively. The two solutions h_p and h_{av} are in relatively good agreement in the region between the initial location $y_0 = 3000$ km (27° N) down to approximately $y = 700$ km (6° N), where the error $h_{error} \equiv |h_{av} - h_p|/H$ was found to be less than 3%. Then, the discrepancy grows rapidly as the current approaches the vicinity of the equator. In this region, the groundings of the numerically calculated height turn rapidly in the downslope direction, while the groundings of h_p do not change their location. The large discrepancy is expected since the geostrophic assumptions are no longer valid in the vicinity of the equator where $f(y)$ becomes vanishingly small (Edwards and Pedlosky 1998, Nof and Borisov 1998, Swaters 2006, 2013, submitted for publication).

The above comparison shows that the numerical solution captures important properties of the Swaters (2013, submitted for publication) analytical results *away* from the equator. Figure 7(b) suggests that the eastward turning is a consequence of the nonlinear terms in the momentum
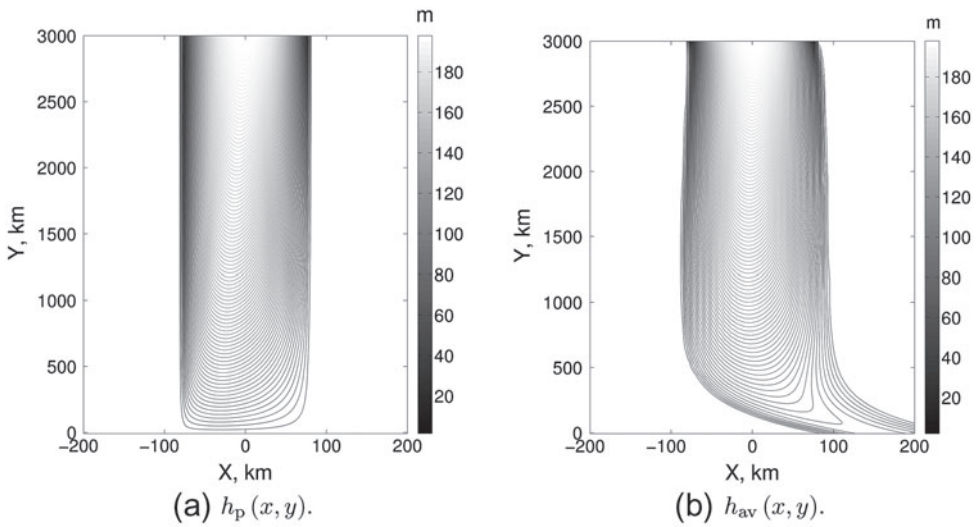
Figure 7. Contour plots of (a) $h_p(x, y)$ as determined by (15) and (16) and (b) $h_{av}(x, y)$ as determined by the numerical simulation for the default parameter values in table 1. The grayscale is proportional to the magnitude of the height in each panel.

equations (which are neglected in the planetary geostrophic approximation) and that the turning takes place in relatively narrow region centered on the equator. Swaters (submitted for publication) has shown that the eastward turning of the equatorward flowing grounded abyssal current is accomplished through the emergence of an "intermediate" equatorial inertial boundary layer of meridional width O (800 km) centered on the equator in which the vv_y term in the meridional momentum equation makes a leading order contribution to the dynamics along with the geostrophic terms.

In the immediate vicinity of the equator between approximately $y = -300$ km and $y = 300$ km, the height of the current does not exceed 20 m. At the same time the eastward velocity, u_{av}, experiences a significant increase on the western side of the channel, reaches its maximum value in the equatorial region of approximately 2 m/s, and then decreases as the fluid approaches the eastern side of the channel. The northward velocity, on the other hand, changes its value in the range between -1.5 m/s and 1.5 m/s as the fluid travels along the equator. In comparison, the average southward speed of the incident current at the northern boundary is 0.08 m/s. This increase in speed as the current approaches the equator is predicted by the Swaters (2013) solution and is a straightforward consequence of maintaining the volume flux within an abyssal current height that is decreasing.

Several other numerical experiments were conducted by changing the value of only one of the control parameters and holding the rest of them equal to their default values. This way we could isolate the effect of each parameter on the behavior of the current.

The meandering of the flow along the equator was observed in all numerical simulations. Hereafter, we refer to this meandering as the "zonal wave". As will be shown later, the wavelength of this zonal wave plays a key role in determining into what hemisphere the current will propagate after its ascent up the eastern slope of the channel.

Varying the reduced gravity, g', in the range between 2×10^{-4} and 32×10^{-4} m/s^2 resulted in the steady solutions for the current's height as shown in figure 8. For each of the four experiments, values of the reduced gravity, inflow volume transport, denoted by Q, and the
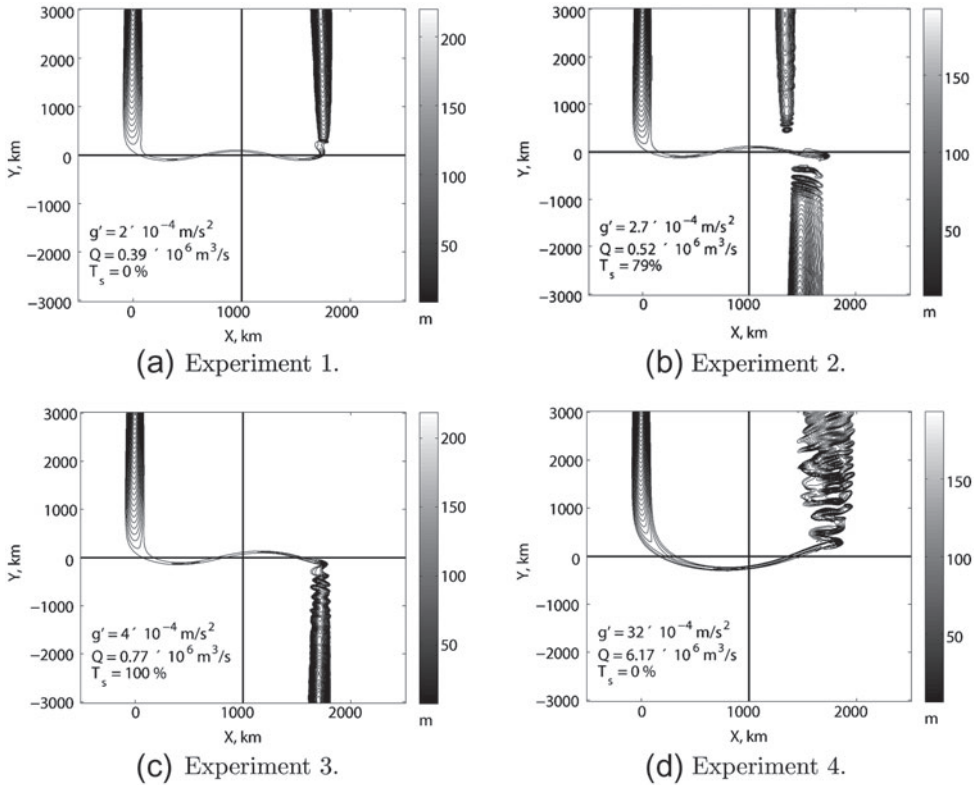
Figure 8. Contour plots for $h_{av}(x, y)$ for the various values of g' listed in table 2. The grayscale is proportional to the magnitude of h_{av}.

fraction (expressed as a percent, which we refer to as the *southward transmission coefficient*) T_s of the source meridional volume flux that ultimately crossed the southern boundary are presented in table 2. Explicitly,

$$T_s \equiv 100\% \times \frac{\int_{x_1}^{x_2} h_{av}(x, -y_0) v_{av}(x, -y_0) \, dx}{\int_{-a}^{a} h_{av}(x, y_0) v_{av}(x, y_0) \, dx}, \tag{17}$$

It is found that for some values of the reduced gravity the structure of the current after its interaction with the equator is completely different from the one presented in figure 6(a). For example, decreasing the reduced gravity by a factor of 4 compared to the default value of $g' = 8 \times 10^{-4} \, \text{m/s}^2$ (see figure 8(a)) made the entire current recirculate back to the northern hemisphere. (The dynamical explanation for this behavior will be given later in this Section).

Table 2. The inflow volume transport Q and transmission coefficient T_s for various g'.

Experiment	$g' \times 10^{-4} \, (\text{m/s}^2)$	Q (Sv)	T_s (%)
1	2	0.39	0
2	2.7	0.52	79
3	4	0.77	100
4	32	6.17	0
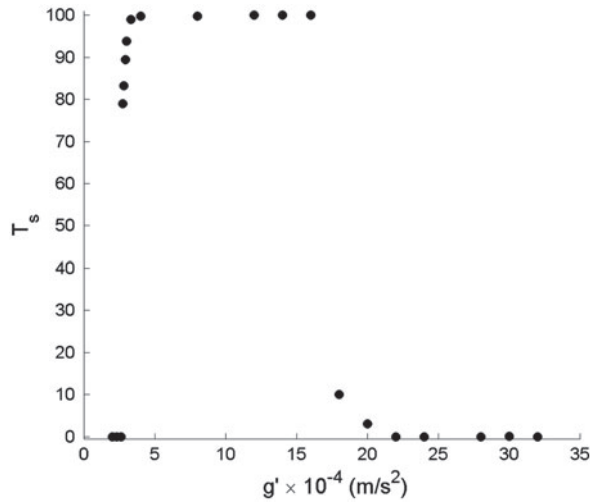
Figure 9.   Southward transmission coefficient T_s (in %) vs. g'.

For $g' = 2.7 \times 10^{-4}$ m/s^2 (see figure 8(b)) we observe the transitional regime, which is characterized by the splitting of the current in two parts after it reaches the maximum run-up point on the eastern side of the channel. The current partially penetrates the southern hemisphere with the remainder returning back to the northern hemisphere. In general, our simulations indicated that, if the splitting does take place, the amounts of fluid that ends up in either hemisphere are very rarely equal.

In most simulations we find the current exits either entirely northward or southward. For example, when $g' = 4 \times 10^{-4}$ m/s^2 (see figure 8(c)), the current exits entirely to the south as in the experiment with the default parameter values. In this case, the picture is not as symmetric because the fluid experiences minor zonal oscillations perpendicular to the direction of the current's propagation after leaving the equatorial region. These oscillations originate when the incident current overshoots the position of geostrophic equilibrium. If the fluid finds itself to be higher upslope than this position, the gravity force acting on it becomes greater than the Coriolis force, therefore making the fluid slide down the slope. Due to inertia, the fluid overshoots the equilibrium position so that the Coriolis force exceeds the gravity force. This process repeats itself until the oscillations disappear due to the process of viscous relaxation. The bulk of the current continues southward with little change in the location of its groundings, similar to the motion of the incident current in the northern hemisphere.

High values of the reduced gravity (see figure 8(d)) make the outflow current switch from the southern hemisphere to the northern hemisphere. In this case, the oscillations of the current as it moves in the northward direction are distinct and are not fully damped by the time the current reaches the northern boundary.

The results of several numerical simulations with different values of the reduced gravity g' are summarized by figure 9, which shows the computed southward transmission coefficient, T_s, vs. the reduced gravity g'. The plot clearly shows a step-like transition from $T_s \approx 0\,\%$ to $T_s \approx 100\,\%$, and from $T_s \approx 100\,\%$ to $T_s \approx 0\,\%$ for $g' \approx 4 \times 10^{-4}$ m/s^2 and $g' \approx 17 \times 10^{-4}$ m/s^2, respectively. We note that the zonal wave increases in wavelength so that a smaller number of waves span the domain as g' increases in this channel of fixed zonal extent. In the analysis that follows, we will show that the ratio of zonal wavelength to zonal extent of the channel determines the transition in T_s.

Numerical simulations were also performed by individually varying other physical parameters (default values are given in table 1). Contours of the current's height in steady-state and of southward transmission coefficients T_s are shown for simulations with varying slope, s, planetary rotation, Ω, zonal channel extent, l, planetary radius, R, incident current half-width, a, and incident current height, H.

All our simulations indicated that the value of the meridional velocity v_{av} at the eastern most point the flow reaches on the eastern slope is rarely zero and plays an important role in determining into what hemisphere the current will penetrate. If the current close to where it completes its ascent up the eastern slope of the channel is heading northward, then it continues northward to the northern boundary. Otherwise, if it is heading southward, it continues southward. All of this is to say that the meridional direction of the current near the eastern slope is set by the phase of the zonal wave at that location. If the maximum southward displacement from the equator is considered a "trough" and the maximum northward displacement a "crest", then the current moves northward if the flow in the zonal wave moves from a trough to crest near the eastern slope. It moves southward if the flow is from a crest to trough instead. In some rare cases, the crests or the troughs of the zonal wave coincide with the location of the maximum run-up point and the meridional velocity v_{av} there has values close to zero. This means that at that point the current did not particularly favor propagation into one or the other of the hemispheres. This situation corresponds to a splitting of the current in two parts following partial recirculation (e.g. see figure 8(b)).

From the range of simulations, we find that varying some parameters (g', s, Ω, l, and R) affects the zonal wave phase at the eastern slope and makes the current switch between the hemispheres, while the variability in other parameters (a and H) has little effect on the final structure of the flow. In particular, increasing g', s and R increases the zonal wavelength, increasing Ω decreases the zonal wavelength and increasing l allows more waves to fit along the zonal extent of the domain.

4. Lagrangian particle models

In order to quantify how the zonal wavelength depends upon g', s, Ω, and R, we examine an idealized "particle-model" for the motion of an equator-crossing fluid parcel. This simplified approach allows us to consider purely inertial motion as it is influenced by rotation and bottom topography while neglecting other complicated effects such as pressure and viscosity.

The question of how the motion of a particle relates to the motion of a fluid parcel in midlatitudes and in the equatorial region is of considerable interest in oceanography and meteorology, and has been extensively studied in the past (e.g. Cushman-Roisin 1982, Paldor and Killworth 1988, Pennell and Seitter 1990, Ripa 1997, Dvorkin and Paldor 1999, Paldor and Sigalov 2006).

The governing equations that describe this motion are given by the four coupled ordinary differential equations

$$\frac{du}{dt} = 2\Omega \sin(y/R)\,v - g'h_b', \qquad \frac{dx}{dt} = u, \qquad (18a,b)$$

$$\frac{dv}{dt} = -2\Omega \sin(y/R)\,u, \qquad \frac{dy}{dt} = v, \qquad (18c,d)$$

where $h_b'(x)$ is the zonal slope of the bottom topography.

We prescribe the initial state of a particle to be analogous to the initial conditions used for numerical simulations of the abyssal current. The particle is placed at $x = 0$ km (the same as the center of the inflow current) and starts its motion from the same latitude $y_0 = 3000$ km in the northern hemisphere with no eastward velocity u. The northward velocity v, on the other hand, is given by the Nof velocity (10). Explicitly, the full set of the initial conditions is given by

$$u|_{t=0} = 0, \qquad\qquad x|_{t=0} = 0, \qquad\qquad (19a,b)$$

$$v|_{t=0} = -v_{\text{nof}}, \qquad\qquad y|_{t=0} = y_0. \qquad\qquad (19c,d)$$

We note that energy is conserved for this model since it follows from (18a–d) that

$$\frac{\mathrm{d}}{\mathrm{d}t} \left(\tfrac{1}{2}u^2 + \tfrac{1}{2}v^2 + g'h_{\text{b}} \right) = 0$$

$$\implies \qquad \tfrac{1}{2}u^2 + \tfrac{1}{2}v^2 + g'h_{\text{b}} = \tfrac{1}{2}u^2(0) + \tfrac{1}{2}v^2(0) + g'h_{\text{b}}(0) = \tfrac{1}{2}v_{\text{nof}}^2,$$

where the initial conditions (19a–d) have been used and that fact, from (6), $h_{\text{b}}(0) = 0$. Energy conservation together with the fact that $h_{\text{b}}'' = s/l > 0$ implies that there must be a finite maximum in the x coordinate of the particle trajectories. It follows from energy conservation that

$$g'h_{\text{b}}(x(t)) = \tfrac{1}{2}v_{\text{nof}}^2 - \tfrac{1}{2}\left[u^2(t) + v^2(t)\right] \leq \tfrac{1}{2}v_{\text{nof}}^2,$$

and since $h_{\text{b}}'' = s/l > 0$ this necessarily implies that $x(t) \leq x_{\max}$ where $h_{\text{b}}(x_{\max}) = v_{\text{nof}}^2/(2g')$ and it is understood that $x_{\max} \geq l$ where $h_{\text{b}}'(l) = 0$.

Despite the seemingly simple structure of the governing equation (18a–d), the particle model has no known explicit analytical solution except where h_{b} is constant in which case the solution can be expressed in terms of elliptic functions (Cushman-Roisin 1982). To gain insight we solved this system numerically varying one physical parameter at a time as was done in the numerical simulations of the abyssal current.

For example, figure 10 shows the trajectories of a particle computed by solving (18a–d) with different values of the reduced gravity. As in the abyssal current numerical simulations, the particle initially travels southward along a straight line parallel to the axis of the channel towards the equator. Upon entering the vicinity of the equator the particle turns eastward in the downslope direction and continues to propagate from west to east oscillating northward and southward about the equator. Eventually, the particle rises up on the eastern side of the channel. In some cases the particle, after it leaves the equatorial region, ends up in one of the hemispheres (see figures 10(a)–(c)). This behavior is similar to that observed in the numerical simulations. Likewise we see that the zonal wavelength increases with increasing g' in these 4 cases.

However, unlike the numerical simulations, the particle model sometimes exhibits chaotic trajectories (see figure 10(c)), switching back and forth between the western and eastern sides of the channel. In spite of this generally chaotic behavior, each individual part of the trajectory is consistent with the trajectories determined for a particle moving along the flat bottom in the equatorial region (Cushman-Roisin 1982, Paldor and Killworth 1988, Ripa 1997, Paldor and Sigalov 2006). Nevertheless, generally speaking (outside of the possibility that chaotic solutions are possible in the particle model), the particle model is able to qualitatively (if not quantitatively) reproduce the fact that whether or not the water mass exhibits complete cross-equatorial motion or recirculates back to the source hemisphere depends on g'.
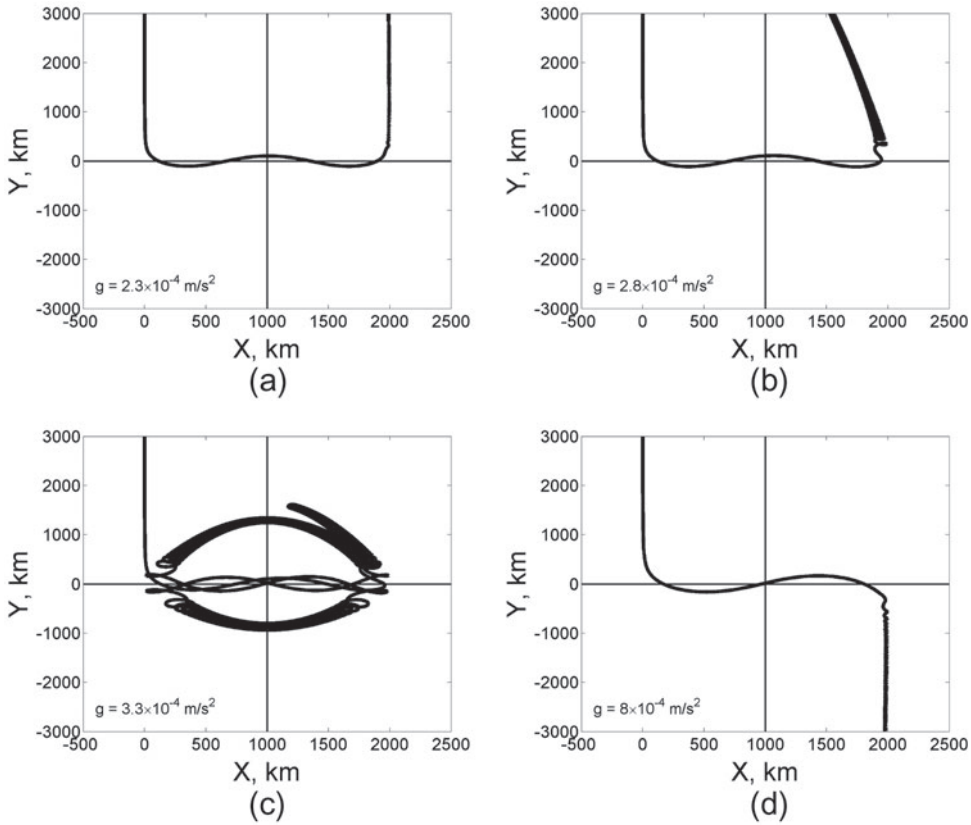
Figure 10.   Trajectories of a particle in the rotating cross-equatorial channel for selected values of g'.

4.1. *Estimating the wavelength of the zonal wave structure*

Because our interest is mainly focused on the zonal wave in the vicinity of the equator, we derived a simplified version of the particle model equation (18a,d) that reveal what combination of the physical parameters defines the wavelength of the zonal wave. (We use the word "wavelength" with caution since the wave structure is not purely periodic in the strict sense of the word.) In order to simplify the equations, we assume the equatorial β-plane approximation to the Coriolis parameter. In addition, we assume that $|y| \sim |v|$ and are both small so that the Coriolis term can be neglected in (18a). The resulting equations are

$$\frac{\mathrm{d}u}{\mathrm{d}t} = -g'h'_{\mathrm{b}} = g's(1 - x/l), \qquad\qquad \frac{\mathrm{d}x}{\mathrm{d}t} = u, \qquad\qquad (20\mathrm{a,b})$$

$$\frac{\mathrm{d}v}{\mathrm{d}t} = -\frac{2\Omega}{R}yu, \qquad\qquad\qquad \frac{\mathrm{d}y}{\mathrm{d}t} = v, \qquad\qquad (20\mathrm{c,d})$$

subject to the following "equatorial" initial conditions

$$u(0) = 0, \qquad\qquad\qquad x(0) = 0, \qquad\qquad (21\mathrm{a,b})$$

$$v(0) = v_0 = \text{constant}, \qquad\qquad y(0) = y_0 = 0. \qquad\qquad (21\mathrm{c,d})$$

The initial conditions (21a–d) differ from differ from (19a–d) in that we set $y(0) = 0$ in (21d) as compared to (19d) and that v_0 is no longer assumed to be the Nof velocity as it is in (19c). This choice is made to be consistent with our underlying assumption/approximation in writing (20a–d) that the zonal wave occurs in a narrow meridional band centered on the equator in which v oscillates about zero, i.e. its average value is essentially zero and does not scale with the Nof speed. It is noted that our principal conclusions are independent of the precise choice of v_0 and y_0 within the context that they must be consistent with the underlying assumptions.

The system (20a–d) can be reduced to

$$\frac{\mathrm{d}^2 u}{\mathrm{d}t^2} + \frac{g's}{l}u = 0, \qquad\qquad x = l - \frac{l}{g's}\frac{\mathrm{d}u}{\mathrm{d}t}, \qquad\qquad (22\text{a,b})$$

$$\frac{\mathrm{d}^2 y}{\mathrm{d}t^2} + \frac{2\Omega}{R}u\,y = 0, \qquad\qquad v = \frac{\mathrm{d}y}{\mathrm{d}t}, \qquad\qquad (22\text{c,d})$$

which has the following solutions for $u(t)$ and $x(t)$, respectively,

$$u(t) = \sqrt{g'sl}\,\sin\left(\sqrt{g's/l}\,t\right), \qquad\qquad x(t) = 2l\sin^2\left(\tfrac{1}{2}\sqrt{g's/l}\,t\right). \qquad (23\text{a,b})$$

In (22a–d) the determination of x and u is no longer coupled to y and v. It follows from (22a) that the appropriate dynamical time scale that determines the zonal position, denoted by T_{eq}, is given by $T_{\mathrm{eq}} = \sqrt{l/(g's)}$. We also note that it follows from (23b) that

$$t = 2\sqrt{\frac{l}{g's}}\,\arcsin\left(\sqrt{\frac{x}{2l}}\right), \qquad\qquad (24)$$

which will be used momentarily. The importance of (24) is that provides the relation that connects time with the zonal coordinate of the particle.

From (23a,b) it follows that at the point of the maximum run-up on the eastern side of the basin the eastward velocity is zero, i.e. $u(T) = 0$ which occurs when $T = \pi\sqrt{l/(g's)}$. Thus, the maximum run-up point, denoted by $x_{\max}$, is given by

$$x_{\max} \equiv x(T) = 2l.$$

The maximum run-up point is symmetrical about the position of maximum depth with respect to the initial position $x(0) = 0$. This is a simple consequence of the "energy" conservation relation

$$\frac{\mathrm{d}}{\mathrm{d}t}\left(\tfrac{1}{2}u^2 + g'h_{\mathrm{b}}\right) = 0$$

$$\implies \qquad \tfrac{1}{2}u^2 + g'h_{\mathrm{b}} = \tfrac{1}{2}u^2(0) + g'h_{\mathrm{b}}(0) = 0,$$

which follows from (20a). Noting that h_{b} is symmetric about $x = l$, it follows that since $u(0) = 0$ the maximum run-up point, where u is also zero, must be located at a value of $x \geq l$ for which $h_{\mathrm{b}}(x) = 0$ and that occurs for $x = 2l$.

To determine the equatorial wave structure we need to determine y. Substitution of (23a) into (22c) leads to the Mathieu equation given by

$$\frac{\mathrm{d}^2 y}{\mathrm{d}t^2} + \frac{2\Omega}{R}\sqrt{g'sl}\,\sin\left(\sqrt{g's/l}\,t\right)y = 0, \qquad\qquad (25)$$

which must be solved subject to

$$y(0) = 0 \qquad \text{and} \qquad \frac{\mathrm{d}y}{\mathrm{d}t}(0) = v_0. \qquad\qquad (26)$$

It is possible to explicitly solve (25) and (26) and determine $y(t)$ in terms of the Mathieu sine and cosine functions (Swaters submitted for publication). It is further possible to determine y as a function of x by substituting (24) into the argument of the Mathieu functions to eliminate t in favor of x. From the resulting complicated expression for $y(x)$ one can numerically determine a "wavelength" for the zonal wave.

Our goal here, however, is to derive a simple *explicit estimate* for the wavelength of the equatorial zonal wave. This can be done as follows. Observing that over the time interval corresponding to the zonal wave, i.e. $0 < t < T = \pi\sqrt{l/(g's)}$, it follows that sin $\left(\sqrt{g's/l}\,t\right) > 0$ in which at $t = 0$ clearly $\sin\left(\sqrt{g's/l}\,t\right) = 0$, which then increases monotonically to $\sin\left(\sqrt{g's/l}\,t\right) = 1$ when $t = T/2$ and then subsequently decreases monotonically back to zero when $t = T$. Consequently, the solution to (25) will be bounded and oscillatory in qualitative behavior over the interval $0 < t < T$. As a simple first approximation for the solution $y(t)$, which avoids working with the Mathieu sine and cosine functions, one can replace $\sin(\sqrt{g's/l}t)$ with its average positive value over the interval $0 < t < T$, which is given by $2/\pi$.

Accordingly, for $0 < t < T$, we approximate (25) with

$$\frac{d^2 y}{dt^2} + \frac{4\Omega}{\pi R}\sqrt{g'sl}\, y = 0, \tag{27}$$

which has the following solution that satisfies (26)

$$y = \left(\frac{v_0}{2} \middle/ \sqrt{\frac{\Omega}{\pi R}\sqrt{g'sl}}\right) \sin\left(2t\sqrt{\frac{\Omega}{\pi R}\sqrt{g'sl}}\right). \tag{28}$$

Then, using (24) we can obtain an approximate expression that describes how the y-coordinate of a particle depends on x over the region corresponding to the zonal wave

$$y = \left(\frac{v_0}{2} \middle/ \sqrt{\frac{\Omega}{\pi R}\sqrt{g'sl}}\right) \sin\left(4\sqrt{\frac{\Omega l}{\pi R}\sqrt{\frac{l}{g's}}} \arcsin\left(\sqrt{\frac{x}{2l}}\right)\right). \tag{29}$$

The oscillating motion described by (29) has a wavelength (over the first cycle), denoted by λ, given by

$$\lambda = 2l \sin^2\left(\frac{\sqrt{\pi^3 R\sqrt{g's}}}{2\sqrt{\Omega}\, l^{3/2}}\right). \tag{30}$$

Since the values of the physical parameters in table 1 are such that the argument of the sine function in (30) is small, it follows that

$$\lambda \approx \pi^3 \frac{R}{2\Omega}\sqrt{\frac{g's}{l}} = \pi^3 L_{eq}, \tag{31}$$

where

$$L_{eq} \equiv \frac{1}{T_{eq}\beta} = \sqrt{g's/l}/\beta,$$

is the zonal length scale characteristic to the equatorial motion of the particle, where $T_{eq} = \sqrt{l/(g's)}$ is the appropriate dynamical time scale for the zonal displacement set by (22a) (equivalently, (24)) and $\beta = 2\Omega/R$ is the equatorial value of the beta-parameter.

Figure 11 compares the estimate (31) to the zonal wavelength measured in the numerical solutions of the particle model (18a–d). This wavelength was determined by estimating twice
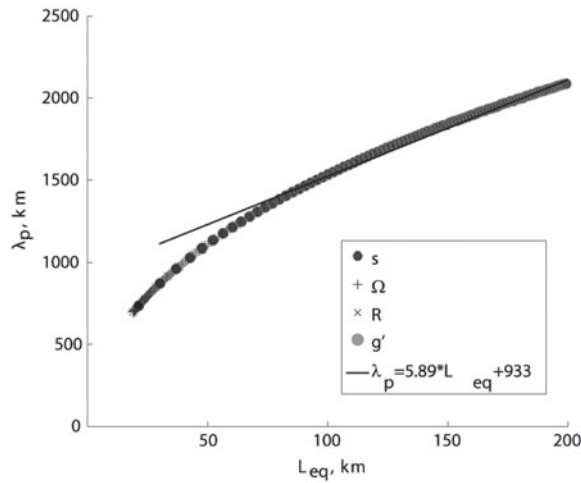
Figure 11.   Wavelength λ_p of the zonal wave as predicted by the particle model (18a–d) vs. the approximate equatorial length scale L_{eq} given by (31). The straight line is the least-squares line given by (32) as computed for the larger values of L_{eq}.

the distance between the first zonal wave crest and trough in each simulation. Figure 11 shows an excellent collapse of data for simulations with widely varying parameters s , Ω, R, and g'.

For sufficiently large L_{eq} we find the zonal wavelength for the particle model, denoted by λ_p, is given approximately by the least-squares fit

$$\lambda_p = 5.89 L_{eq} + \lambda_0, \qquad \text{with} \qquad \lambda_0 = 933\,\text{km}. \tag{32}$$

The slope of 5.89 in (32) is to be compared with the slope of $\pi^3 \simeq 31$ in (31). However, the slope of 5.89 in (32) was computed for the larger L_{eq} values where presumably the Taylor expansion used in going from (30) to (31) starts to lose its validity. As can be seen in figure 11 for smaller values of L_{eq}, the slope associated with the data points is larger.

4.2. *Comparison between the particle model and the numerical simulation*

Similarly, we anticipate that the zonal wavelength seen in the abyssal current numerical simulations should depend upon the equatorial length scale. For each shallow water numerical simulation of the abyssal current a wavelength, denoted by λ_s, was determined by estimating twice the distance between the first zonal wave crest and trough and was plotted against L_{eq} (see figure 12). Figure 12 shows that the measured wavelength in the numerical simulation of the zonal wave formed by the current in the equatorial region is well predicted by L_{eq}.

All points in figure 12 show an almost linear increase of the wavelength λ_s with L_{eq}. A least-squares line though these data points was determined that gives

$$\lambda_s = 10.7 L_{eq} + \lambda_0, \qquad \text{with} \qquad \lambda_0 = 779\,\text{km}. \tag{33}$$

The slope of 10.7 in (33) is approximately twice as large as that in (32) and closer to the approximate estimate in (31).

Earlier we argued that the position of the maximum run-up point relative to the crest and troughs of the zonal wave (i.e. the ratio between the zonal wavelength λ_s and the width of the
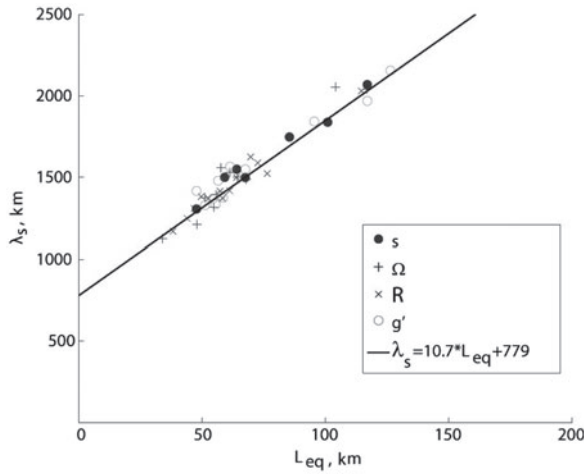
Figure 12. Wavelength λ_s of the zonal wave in the equatorial region as determined by the shallow water numerical simulations vs. the equatorial length scale L_{eq} given by (31). The straight line is the least-squares line as determined by (33).
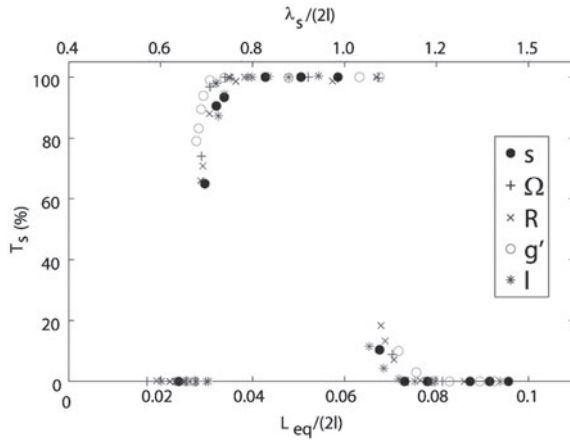
Figure 13. Southward transmission coefficient T_s vs. $\lambda_s/(2l)$ (top axis) and $L_{eq}/(2l)$ (bottom axis).

topography $2l$) is ultimately responsible for determining the hemisphere into which the current will eventually flow into. Our hypothesis is strongly supported by figure 13, which shows the percentage of the fluid that flows southward depends on the phase of the wave expressed by the ratio $\lambda_s/2l$ (top axis) and $L_{eq}/2l$ (bottom axis). The combination of values of T_s determined from all the shallow water numerical simulations collapse to form a well-defined step-like curve. The fact that the initial half-width and maximum height (a and H) of the current are not present in the equatorial length scale indicates that the zonal wavelength and, consequently, the percentage of the fluid that crossed the equator southward are also independent of a and H, consistent with our simulations.

For relatively small and large values of $\lambda_s/(2l)$ in figure 13, the current experiences full recirculation back into the northern hemisphere (i.e. $T_s \approx 0\%$). These values correspond to

the physical situations when the zonal channel contains between 1/4 to about 3/4 or about 5/4 to about 7/4 wavelengths (e.g. figures 8(a) and (d), respectively) of the zonal wave. In these cases, the eastern run-up point occurs *after* a trough of the zonal wave and *before* its next crest and has a positive meridional velocity. However, if the channel contains between about 3/4 to about 5/4 wavelength of the zonal wave, then the run-up point occurs *after* a crest and *before* the next trough (e.g. figure 8(c)) where the meridional velocity is negative, and the entire current ends up in the southern hemisphere (i.e. $T_s \approx 100\%$). Although we did not run numerical simulations for parameter values corresponding to larger values of $\lambda_s/(2l)$, the clear implication of our work would be that if $7/4 < \lambda_s/(2l) < 9/4$, for example, then the entire current would end up in the southern hemisphere. This pattern of the flow switching back and forth between $T_s \approx 0\%$ and $T_s \approx 100\%$ would continue, in principle, as $\lambda_s/(2l)$ increases.

From figure 13 we estimate that there are two relatively narrow transitional regions corresponding to the situation where the current ultimately splits into a portion flowing into the northern *and* southern hemispheres: $\lambda_{s_1}/(2l) \approx 0.68$ and $\lambda_{s_2}/(2l) \approx 1.13$ (e.g. figure 8(b)). We argue that 0.68 and 1.13, all things considered, are "close" to 3/4 and 5/4, respectively. Considering the fact that (31) is derived from the much simplified particle model (20a–d), surprisingly good agreement is seen in figure 13 in the location of the transitional regions between the different sets of the numerical simulations considered as a function of L_{eq}.

5. Discussion and conclusions

Numerical simulations have shown that when equatorward-flowing currents approach the equator on the western side of the basin with parabolic bottom topography they deflect toward the east and subsequently oscillate meridionally until reaching a maximum run-up point on the eastern side of the basin. Thereafter they move, generically, entirely northward or southward depending on the what the phase of the zonal wave is at the maximum run-up point on the eastern side. If the eastern run-up point occurs *after* a trough of the zonal wave and *before* its next crest, then flow recirculates back into the northern hemisphere. If the eastern run-up point occurs *after* a crest of the zonal wave and *before* its next trough, the flow moves entirely into the southern hemisphere.

For the range of parameter values that we examined in our shallow water numerical simulations, we found that the zonal wavelength of the along-equatorward flow is a linear function of the equatorial length scale. In addition, we found that the southward transmission coefficient, denoted as T_s, and determined as the percentage volume fraction of water that exits the southern boundary is set by the number of wavelengths that can fit into the zonal extent of the topography. Our simulations showed that the transitions between $T_s \approx 0\%$ and $T_s \approx 100\%$ were fairly sharply defined and the extent of the transitional regions was found to be much narrower than those described by Nof and Borisov (1998). The reason for this difference is not exactly clear. It may be that our numerical simulations had higher spatial resolution or other differences in our approach to the numerical solution of the shallow water equations. It may simply be that we had more parameter data points to work with and these more clearly defined the transitional regime.

It is of interest to try to estimate what our model calculation says about the DWBC in the north Atlantic. Although there is considerable variability and uncertainty, oceanographically observed estimates for the order of magnitudes for the parameters of deep currents in the

Atlantic at 26.5° N ($y_0 \approx 2900$ km) (e.g. Haak *et al.* 2007, Peña-Molino *et al.* 2012, Meinen *et al.* 2013) are about $g' \approx 0.002$ m/s^2 and $s \approx 0.008$. Taking the radius and rotation of the Earth to be $R \approx 6371$ km and $\Omega \approx 7.3 \times 10^{-5}$ rad/s, respectively, and estimating $2l = 2500$ km to be the zonal extent of equatorial Atlantic, we calculate that $L_{eq}/2l \approx 0.069$. Hence, the relative zonal wavelength is predicted to be $\lambda_s/2l \approx 1.06$. All our models would predict (see figure 13) full penetration of the abyssal current into the southern hemisphere. However, in this case the current's state is described by the point located near the transition at $\lambda_s/2l$, which means that even a slight increase in $\lambda_s/2l$, for example through shortening of the zonal extent l by the influence of the Mid-Atlantic Ridge, might dramatically change the pathway of the abyssal current. Hopefully, this contribution has offered some explanation for the possible mechanisms of the observed recirculation of North Atlantic Deep Water as it approaches the equator (McCartney 1993, McCartney and Curry 1993, Schmid *et al.* 2005, Sarafanov *et al.* 2007).

The model presented in this paper uses a highly idealized topography and shape of the abyssal current. We hope that future numerical simulations will take into account some important phenomena that take place in the real ocean, but are omitted in our model. In order to improve this model, one might consider the analysis of multi-layered or continuously stratified models with the implementation of some important features such as a more realistic topography, mixing, turbulent effects, etc. For example, it is argued that taking into account the horizontal component of the Earth's rotation vector will increase the cross-equatorial transport by 10–30 % (Stewart and Dellar 2012). Including all of the above-mentioned processes in a numerical model might reveal alternative recirculation mechanisms in the abyss of the world oceans.

Acknowledgements

References

Arakawa, A. and Hsu, Y.J.G., Energy conserving and potential-enstrophy dissipating schemes for the shallow water equations. *Mon. Weather Rev.* 1990, **118**, 1960–1969.

Arakawa, A. and Lamb, V.R., Computational design of the basic dynamical processes of the UCLA general circulation model. *Methods Comput. Phys.* 1977, **17**, 173–265.

Borisov, S. and Nof, D., Deep, cross-equatorial eddies. *Geophys. Astrophys. Fluid Dyn.* 1998, **87**, 273–310.

Choboter, P.F. and Swaters, G.E., Modeling equator-crossing currents on the ocean bottom. *Can. Appl. Math. Quart.* 2000, **8**, 367–385.

Choboter, P.F. and Swaters, G.E., Two-layer models of abyssal equator-crossing flow. *J. Phys. Oceanogr.* 2003, **33**, 1401–1415.

Choboter, P.F. and Swaters, G.E., Shallow water modeling of Antarctic bottom water crossing the equator. *J. Geophys. Res.* 2004, **109**, C03038.

Cunningham, S.A., Kanzow, T., Rayner, D., Baringer, M.O., Johns, W.E., Marotzke, J., Longworth, H.R., Grant, E.M., Hirschi, J.J.M., Beal, L.M., Meinen, C.S. and Bryden, H.L., Temporal variability of the Atlantic meridional overturning circulation at 26.5 N. *Science* 2007, **317**, 935–938.

Curry, J.H. and Winsand, D., Low-order intermediate models: Bifurcation, recurrence and solvability. *J. Atmos. Sci.* 1986, **43**, 2360–2373.

Cushman-Roisin, B., Motion of a free particle on a beta-plane. *Geophys. Astrophys. Fluid Dyn.* 1982, **22**, 85–102.

De Madron, X.D. and Weatherly, G., Circulation, transport and bottom boundary layers of the deep currents in the Brazil Basin. *J. Mar. Res.* 1994, **52**, 583–638.

Dvorkin, Y. and Paldor, N., Analytical considerations of Lagrangian cross-equatorial flow. *J. Atmos. Sci.* 1999, **56**, 1229–1237.

Edwards, C.A. and Pedlosky, J., Dynamics of nonlinear cross-equatorial flow. Part I: Potential vorticity transformation. *J. Phys. Oceanogr.* 1998, **28**, 2382–2406.

Gent, P.R., The energetically consistent shallow-water equations. *J. Atmos. Sci.* 1993, **50**, 1323–1325.

Gent, P.R. and McWilliams, J.C., Intermediate model solutions to the Lorenz equations: Strange attractors and other phenomena. *J. Atmos. Sci.* 1982, **39**, 3–13.

Gustafsson, B. and Sundstrom, A., Incompletely parabolic problems in fluid dynamics. *SIAM J. Appl. Math.* 1978, **35**, 343–357.

Haak, H., Baehr, J., Jungclaus, J., Cunningham, S. and Marotzke, J., Observed and simulated daily to seasonal MOC variability at 26N in the Atlantic. *Geophys. Res. Abstr.* 2007, **9**, 09574.

Kawase, M., Rothstein, L.M. and Spriinger, S.R., Encounter of a deep western boundary current with the equator: A numerical spin-up experiment. *J. Geophys. Res.* 1992, **97**, 5447–5463.

Killworth, P.D., Cross-equatorial geostrophic adjustment. *J. Phys. Oceanogr.* 1991, **21**, 1581–1601.

Kim, A., Cross-equatorial flow of grounded abyssal ocean currents. M.Sc. Thesis, University of Alberta, Canada, 2013, pp. 80.

Kirkpatrick, M.P. and Armfield, S.W., Open boundary conditions in numerical simulations of unsteady incompressible flow. *ANZIAM J.* 2009, **50**, C760–C773.

Lorenz, E.N., Attractor sets and quasi-geostrophic equilibrium. *J. Atmos. Sci.* 1980, **37**, 1685–1699.

MacCormack, R. and Paullay, A., Computational efficiency achieved by time splitting of finite difference operators. *AIAA J.* 1972, Paper 72–154.

McCarthy, G., Frajka-Williams, E., Johns, W., Baringer, M., Meinen, C., Bryden, H., Rayner, D., Duchez, A., Roberts, C. and Cunningham, S., Observed interannual variability of the Atlantic meridional overturning circulation at 26.5 N. *Geophys. Res. Lett.* 2012, **39**, L19609.

McCartney, M.S., Crossing of the equator by the deep western boundary current in the western Atlantic Ocean. *J. Phys. Oceanogr.* 1993, **23**, 1953–1974.

McCartney, M.S. and Curry, R.A., Transequatorial flow of Antarctic bottom water in the western Atlantic Ocean: Abyssal geostrophy at the equator. *J. Phys. Oceanogr.* 1993, **23**, 1264–1264.

McDonald, P., The computation of transonic flow through two-dimensional gas turbine cascades. *ASME* 1971, Paper 71-GT-89.

Meinen, C.S., Johns, W.E., Garzoli, S.L., van Sebille, E., Rayner, D., Kanzow, T. and Baringer, M.O., Variability of the Deep Western Boundary Current at 26.5 N during 2004–2009. *Deep-Sea Res. II* 2013, **85**, 154–168.

Nof, D., The translation of isolated cold eddies on a sloping bottom. *Deep-Sea Res.* 1983, **30**, 171–182.

Nof, D. and Borisov, S., Inter-hemispheric oceanic exchange. *Q. J. Roy. Meteor. Soc.* 1998, **124**, 2829–2866.

Nof, D. and Olson, D.B., How do western abyssal currents cross the equator? *Deep-Sea Res.* 1993, **40**, 235–255.

Paldor, N. and Killworth, P.D., Inertial trajectories on a rotating earth. *J. Atmos. Sci.* 1988, **45**, 4013–1019.

Paldor, N. and Sigalov, A., Inertial particle approximation to solutions of the shallow water equations on the rotating spherical Earth. *Tellus A* 2006, **58**, 280–292.

Peña-Molino, B., Joyce, T.M. and Toole, J.M., Variability in the deep western boundary current: Local versus remote forcing. *J. Geophys. Res.* 2012, **117**, C12022.

Pennell, S.A. and Seitter, K.L., On inertial motion on a rotating sphere. *J. Atmos. Sci.* 1990, **47**, 2032–2034.

Ripa, P., Inertial oscillations and the β-plane approximation(s). *J. Phys. Oceanogr.* 1997, **27**, 633–647.

Samelson, R.M., *The Theory of Large-scale Ocean Circulation*, 2011 (Cambridge, UK: Cambridge University Press).

Sandoval, F.J. and Weatherly, G.L., Evolution of the deep western boundary current of Antarctic bottom water in the Brazil Basin. *J. Phys. Oceanogr.* 2001, **31**, 1440–1460.

Sarafanov, A., Sokov, A. and Demidov, A., Water mass characteristics in the equatorial North Atlantic: A section nominally along 6.5 N, July 2000. *J. Geophys. Res.* 2007, **112**, C12023.

Schmid, C., Bourles, B. and Gouriou, Y., Impact of the equatorial deep jets on estimates of zonal transports in the Atlantic. *Deep-Sea Res. II* 2005, **52**, 409–428.

Siedler, G., Church, J., Gould, J. and Griffies, S., *Ocean Circulation and Climate: Observing and Modelling the Global Ocean*, 2001 (New York: Elsevier).

Stephens, J.C. and Marshall, D.P., Dynamical pathways of Antarctic bottom water in the Atlantic. *J. Phys. Oceanogr.* 2000, **30**, 622–640.

Stevens, D.P., On open boundary conditions for three dimensional primitive equation ocean circulation models. *Geophys. Astrophys. Fluid Dyn.* 1990, **51**, 103–133.

Stewart, A. and Dellar, P., Cross-equatorial channel flow with zero potential vorticity under the complete Coriolis force. *IMA J. Appl. Math.* 2012, **77**, 626–651.

Swaters, G.E., The meridional flow of source-driven abyssal currents in a stratified basin with topography. Part 1: Model development and dynamical properties. *J. Phys. Oceanogr.* 2006, **36**, 335–355.

Swaters, G.E., Flow of grounded abyssal ocean currents along zonally-varying topography on a rotating sphere. *Geophys. Astrophys. Fluid Dyn.* 2013, **107**, 564–586.

Swaters, G.E., The steady midlatitude-equatorial dynamics of a grounded deep-western boundary current in a meridional basin with parabolic bottom topography. *J. Fluid Mech.* submitted for publication.